

Alpha scattering from ^{209}Bi at 50.5 MeV

A. Chatterjee, S. K. Gupta, S. Kailas, and S. S. Kerekatte

Nuclear Physics Division, Bhabha Atomic Research Centre, Trombay, Bombay 400085, India

(Received 14 September 1987)

The cross sections for the elastic and inelastic scattering of alpha particles from ^{209}Bi have been measured at 50.5 MeV for angles up to 92° in steps of 1° . An optical model analysis of the elastic scattering data has been made, starting with the parameters predicted from systematics and consistent with those determined at higher energies. The large angular range combined with the relatively small errors in the measurement restrict the real potential to just three discrete families. A nearside-farside decomposition of the data clearly reveals the Fraunhofer diffraction pattern superimposed on the large background of Fresnel diffraction. The inelastic scattering data have been analyzed in terms of the collective model using the distorted wave Born approximation, for which the distorted waves were generated by the optical model analysis of the elastic scattering data. The values of the deformation lengths (βR) obtained are compared with those reported in the literature.

I. INTRODUCTION

The study of elastic scattering of a particle incident on a nucleus is a basic ingredient for understanding other more complicated reaction processes, such as transfer reactions, the formation of compound nuclei, and their various decay modes. The analysis of the differential cross sections for elastic scattering provides a simple handle to determine the interaction between nuclei. Phenomenologically, this interaction is parametrized in terms of the complex optical potential with a Woods-Saxon geometry.

Although alpha scattering has been studied extensively,¹ the optical model parameters deduced are not unique except at higher energies² ($E_\alpha > 90$ MeV) where nuclear rainbow scattering³ is observed. At low energies the analysis suffers from the Igo⁴ ambiguity (determining the potential only at the strong absorption radius) and the discrete potential ambiguity.^{5,6}

The present measurement of alpha scattering from ^{209}Bi has been carried out with the aim of reducing the ambiguities in the optical potential by measuring the data accurately over a wide angular range. In Sec. II the experimental procedure and the angular distribution results for elastic and inelastic scattering are presented. In Sec. III a detailed discussion of the optical model analysis is given. From the systematics of the alpha-nucleus optical model parameters established earlier,⁷⁻⁹ the parameters relevant to the $^{209}\text{Bi} + ^4\text{He}$ system at 50.5 MeV are deduced. These initial parameters are then fine tuned to get the best fit to the data. The notch perturbation test¹⁰ has been carried out to determine the radial region of sensitivity. The discrete family ambiguity, combined with the surface ambiguity, has been studied. A nearside-farside decomposition^{11,12} of the data has been made. The nearside-farside analysis prominently features the Fraunhofer oscillations at large angles which are due to the interference of the near and the far amplitudes. In Sec. IV the data for the inelastic scatter-

ing to the low lying states in ^{209}Bi are compared with distorted wave Born approximation (DWBA) calculations employing the optical parameter set which best fits the elastic data. The deduced deformation parameters are then compared with those from other measurements.

II. EXPERIMENTAL PROCEDURE AND RESULTS

The measurement was made using the unanalyzed 50.5 alpha-particle beam from the 224 cm variable energy cyclotron at Calcutta. The target was located at the center of the 90 cm diameter scattering chamber. The collimator geometry used for the beam transport into the chamber was chosen to optimize the beam transmission.¹³ For the collimation three slits were used. The first slit of 8 mm diameter was followed by a second slit of 2 mm diameter with a spacing of 1.5 m between them. This was followed by a third (antiscattering) slit of 6 mm diameter at a distance of 41 cm from the second collimator. The target was 9 cm downstream of the third slit. This geometry sets an acceptance of 10.6 mm mrad with a beam size of less than 6 mm.

The measured data are shown in Fig. 1 plotted as σ/σ_R , where σ_R is the Rutherford cross section. In order to minimize systematic errors in σ/σ_R , it is important to determine the beam energy and the detector angles accurately. The three collimators were optically aligned to ensure an angular offset of less than $\pm 0.2^\circ$. The angular offset of the two detector arms was checked optically and found to be better than $\pm 0.05^\circ$. The angular offset of the detectors was checked independently using a Mylar [$(\text{C}_{10}\text{H}_8\text{O}_4)_n$] target and locating the two peaks in the energy spectra, arising due to alpha scattering from hydrogen, as a function of angle. The energy difference approaches zero as the maximum kinematically allowed angle, θ_{max} , is approached. The calculated value of θ_{max} for the alpha-H system is 14.7° , independent of the bombarding energy. The measured angular offset by this method was less than $\pm 0.07^\circ$. The ratio of

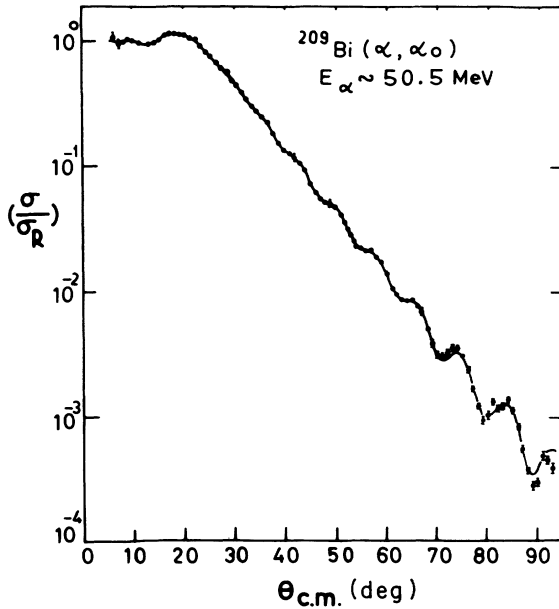


FIG. 1. The ratio of the elastic scattering cross sections to the Rutherford cross sections plotted as a function of the center-of-mass angle. The solid line is the optical-model fit to the data with the final values of the parameters given in Table I.

the $^{209}\text{Bi} + ^4\text{He}$ elastic cross sections at 5° and 6° , assuming them to be purely due to Rutherford scattering, was used as a further check on the angular accuracy, determining the offset to be less than $\pm 0.1^\circ$.

Targets in the form of self-supporting foils of natural bismuth metal were prepared by vacuum evaporation. The thicknesses of the two targets used, determined by the energy shift of ^{241}Am alpha peaks, were 1.00 and 2.33 mg/cm^2 .

Two Si detectors of thicknesses 2 mm and 3 mm, subtending solid angles of 0.149 and 0.229 msr, respectively, were used. The overall resolution was 200 keV. A 5 mg/cm^2 thick Al foil, placed in front of the detectors to stop fission fragments, considerably improved the spectra for $\theta > 50^\circ$. Absolute cross sections were determined by measuring the detector solid angles and the current integrator calibration. In addition to the current integrator, a monitor detector at 32° was used as a check on the point-to-point normalization.

From a spectrum using a Mylar target, the beam energy E_α was determined accurately from kinematics. This was done using the channel positions $N(^{16}\text{O})$ and $N(^{12}\text{C})$ of the elastic alpha peaks from ^{16}O and ^{12}C scattering and the channel position, $N(^{12}\text{C}^*)$ of one of the inelastic alpha peaks from ^{12}C scattering (4.439 or 9.641 MeV). The expression used is

$$E_\alpha = \frac{N(^{16}\text{O}) - N(^{12}\text{C})}{N(^{12}\text{C}) - N(^{12}\text{C}^*)} K(E_\alpha), \quad (1)$$

where $K(E_\alpha)$ is a slowly varying function of E_α . Equation (1) is applied iteratively starting from an approxi-

mate value of E_α and the convergence is rapid. For a given detector angle θ and beam energy E_α , the energies $E(^{16}\text{O})$, $E(^{12}\text{C})$, and $E(^{12}\text{C}^*)$ corresponding to the peak positions can be predicted using relativistic kinematics and $K(E_\alpha)$ can be calculated as

$$K(E_\alpha) = \frac{E(^{12}\text{C}) - E(^{12}\text{C}^*)}{E(^{16}\text{O}) - E(^{12}\text{C})} E_\alpha. \quad (2)$$

At $\theta = 60^\circ$ and considering the 4.439 MeV state in ^{12}C , for example, $K(E_\alpha)$ varies from 61.970 to 59.338 MeV when E_α varies from 10 to 120 MeV. The slow variation of $K(E_\alpha)$ enables an application of (1) to determine E_α even when the approximate beam energy is not known in advance. For the present measurement, E_α was estimated to be (50.54 ± 0.04) MeV.

The elastic scattering angular distribution was measured in steps of 1° covering the angular range 5° to 92° . The measured σ/σ_R values vary from 1 to 3×10^{-4} . Beyond $\theta \sim 60^\circ$, oscillations are clearly seen in the angular distribution. Typical errors on the σ/σ_R values vary from 3–5% below 70° to 5–10% for angles beyond 70° .

The measured cross sections for the inelastic scattering to the states of 2.60 and 4.22 MeV are shown in Fig. 2. The yields from the other states were generally small. Because of the presence of oxygen and carbon as target contaminants, the cross sections were extracted only for $\theta > 30^\circ$ and $\theta < 40^\circ$, respectively, for the states at $E^* = 2.60$ and 4.22 MeV.

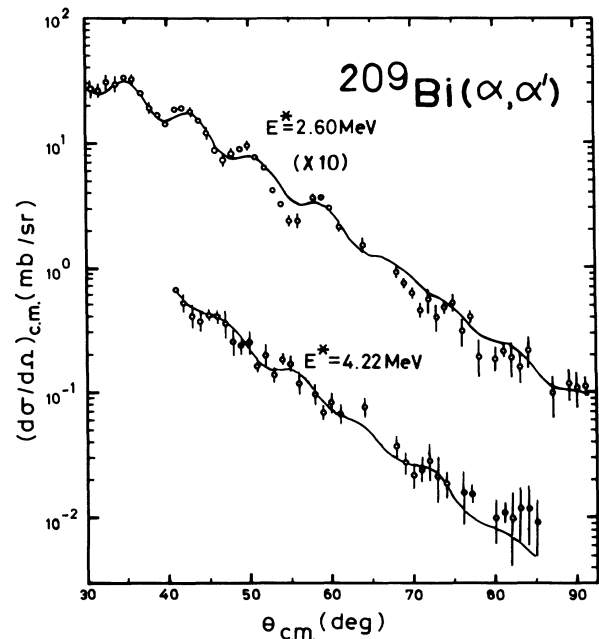


FIG. 2. Cross sections for the inelastic scattering to the states at 2.60 and 4.22 MeV plotted as a function of the center-of-mass angle. The solid lines are calculated using the DWBA formalism as discussed in the text.

III. ANALYSIS

A. Elastic scattering

The elastic scattering angular distribution has been analyzed using the optical model and the computer code SNOOPY.¹⁴ The optical potential employed is parametrized as

$$V(r) = V_{\text{Coul}}(r) - V_R f_R(r) - iV_I f_I(r), \quad (3)$$

where V_{Coul} is the usual Coulomb potential with Coulomb radius $R_C = 1.3 A_T^{1/3}$ fm (A_T is the target mass number); V_R and V_I are the strengths of the real and the imaginary parts, respectively. The form factor is given as

$$f_x = 1 / \{1 + \exp[(r - R_x)/a_x]\}, \quad (4)$$

where $x = R$ or I .

As the analysis of the data at these relatively low energies ($E_\alpha = 50.5$ MeV) suffers from discrete family ambiguities (in particular for the real part of the potential) we followed the procedure of extrapolating to lower energies the "unique" real potential parameters determined at higher energies with suitable energy variation. For doing this effectively we have made use of the systematics⁸ of the volume integral,

$$J_R = \frac{1}{4} \frac{4\pi}{3A_T} V_R R_R^3 (1 + \pi^2 a_R^2 / R_R^2), \quad (5)$$

the $R_{2.4}$ radius (where the potential becomes 2.4 MeV) defined as

$$R_{2.4} = a_R \ln[(V_R - 2.4)/2.4] + R_R, \quad (6)$$

and the slope, S , at $r = R_{2.4}$,

$$S = \frac{1}{a_R} \{1 + \exp[-(R_{2.4} - R_R)/a_R]\}^{-1}. \quad (7)$$

A global formula⁷ which fits the J_R data for alpha particles is

$$J_R = J_0 (1 + c A_T^{-1/3}) \text{ MeV fm}^3, \quad (8)$$

where

$$J_0 = 318.5 - 2.19E - 124.2 \times 3 \exp(-0.8 \times 4^{1/3} - 0.012E)$$

with $E(\text{MeV}) = (E_{\text{c.m.}} - 1.44 \times 2Z_T / A_T^{1/3} - 28.3)/4$ and $c = 2$. The corresponding formulae⁸ for $R_{2.4}$ and S are

$$R_{2.4}(\text{fm}) = 2.965 + 1.257 A_T^{1/3} \quad (9)$$

and

$$S(\text{fm}^{-1}) = 1.627 - 0.0024 E_\alpha. \quad (10)$$

As discussed in Ref. 8, by combining J_R , $R_{2.4}$, and S , it is possible to predict V_R , R_R , and a_R of the real part. For the $^{209}\text{Bi} + ^4\text{He}$ system at $E_\alpha = 50.5$ MeV, these values are given in Table I.

For the imaginary part also we have the corresponding systematics of J_I , $R_{2.4}$, and S values, using the potential parameters from Ref. 15. A global formula for J_I has been given⁹ as

$$J_I = 43.4 (1 + 5 A_T^{-1/3}) [1 - \exp(-\alpha E_{\text{c.m.}})], \quad (11)$$

where $\alpha = 0.03 \text{ MeV}^{-1}$. In Fig. 3 the systematics for $R_{2.4}$ and S are displayed. These quantities can be represented as

$$R_{2.4}(\text{fm}) = (1.333 + 1.503 A_T^{1/3}) \times [1 - \exp(-0.11 E_\alpha)], \quad (12)$$

$$S(\text{fm}^{-1}) = 1.912 - 0.00226 E_\alpha. \quad (13)$$

TABLE I. Initial and final values of optical model parameters and related quantities.

	Initial values		Final values
	Real part		
V_R (MeV)		108	111
r_R (fm)		1.343	1.343
a_R (fm)		0.649	0.649
J_R (MeV fm ³)		292	300
$R_{2.4}$ (fm)		10.425 ^a	10.444
S (fm ⁻¹)		1.507	1.508
R_{rms} (fm)		6.628	6.628
	Imaginary part ^b		
	Prescription 1	Prescription 2	
V_I (MeV)	14.2	18.9	16
r_I (fm)	1.597	1.431	1.454
a_I (fm)	0.462	0.692	0.79
J_I (MeV fm ³)	62	62	56
$R_{2.4}$ (fm)	10.211		9.999
S (fm ⁻¹)	1.799		1.076
R_{rms} (fm)	7.539	7.063	7.300

^a $R_{2.4}$ and S are the radius and slope at the point where the potential becomes 2.4 MeV.

^bFor the imaginary part two prescriptions were used to predict the initial parameter values (see text for details).

As before, by combining these quantities, we can predict the parameters of the imaginary potential. These values are given in Table I (prescription 1).

We have also used an alternate prescription to predict the parameters of the imaginary potential. It has been found (Fig. 4) that the ratio of the rms radii of the imaginary and the real parts of the potential also has a simple parametric representation which is approximately independent of the target nucleus. The relation is given as

$$R_{IR}(\text{fm}) = 1 + 0.13[1 - \exp(-0.014E_\alpha)] . \quad (14)$$

Further assuming $R_I = R_{IR}R_R$, $a_I = R_{IR}a_R$, and with J_I predicted from (11), it is possible to get the imaginary potential parameters. These values are also listed in Table I (prescription 2).

In essence, by the prescriptions mentioned above we have all the parameters predicted for the $^{209}\text{Bi} + ^4\text{He}$ system at $E_\alpha = 50.5$ MeV and these are consistent with the ones determined at higher E_α . Starting with these parameters, we have optimized the fit to the data by variation of the parameters and the usual χ^2 minimization

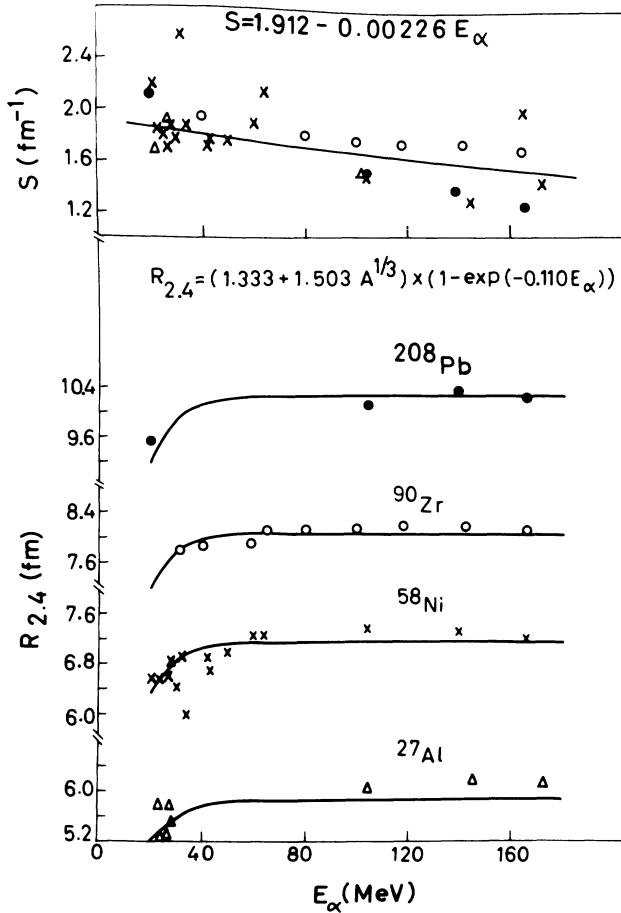


FIG. 3. Systematics for $R_{2.4}$ and S (as defined in the text) for the alpha-nucleus imaginary potential for the targets ^{208}Pb (solid circles), ^{90}Zr (open circles), ^{58}Ni (crosses), and ^{27}Al (triangles) in the alpha energy range 20–170 MeV. The solid lines are empirical fits to the data with the functional forms indicated.

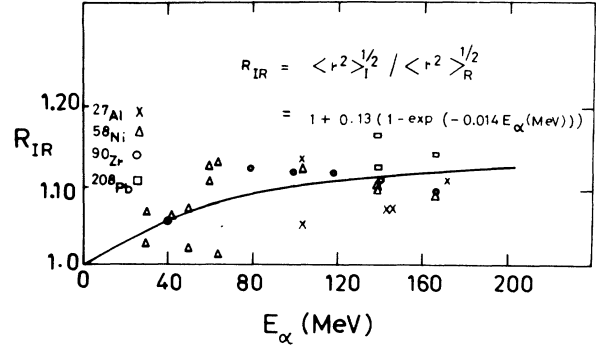


FIG. 4. Ratio of the rms radii of the imaginary and the real parts of the alpha-nucleus optical potential plotted as a function of alpha energy. The solid line is an empirical fit with the functional form indicated.

criterion. The predicted imaginary potential parameters are slightly different for the two prescriptions; however, the same final parameters are obtained by starting with either set. The final set of parameters and related quantities are listed in Table I. The fit to the data is shown in Fig. 1 and the quality of the fit is quite good except at the extreme backward angles. It may be noted that the final set of values for the real potential parameters and the volume integral J_R are nearly the same as the ones we started with. However, the imaginary potential parameters have changed considerably, even though J_I has not changed appreciably. The reaction cross section determined by the optical model is $\sigma_R = 2234$ mb.

The l value at which the alpha transmission coefficient becomes 0.5 is usually identified as l_{SA} . Using this the strong absorption radius R_{SA} can be calculated with the expression

$$R_{SA} = (\eta/k) \{ 1 + [1 + (l_{SA} + \frac{1}{2})^2 / \eta^2]^{1/2} \} , \quad (15)$$

where η and k have the usual meaning. In the present case $l_{SA} = 24.7$ and $R_{SA} = 11$ fm.

1. Notch perturbation test

A radial notch perturbation test¹⁰ has been carried out to determine the region of the potential most sensitive in predicting the elastic scattering data. The procedure is to introduce a radial perturbation into the potential in a localized radial region and to observe its effect on the predicted cross sections. It is then concluded that a region of the potential is least (most) sensitive to the data if a perturbation in this region has a weak (strong) effect on the cross section. This can be done by comparing the experimental data with the calculations and by calculating χ^2 as the perturbing potential is moved along the radial region. In the present work we have used the perturbing potential (for the real R and imaginary I parts)

$$V_p(r) = V_{R(I)} f_{R(I)} \{ 1 - 4f_p(r)[1 - f_p(r)] \} , \quad (16)$$

where

$$f_p(r) = 1 / \{ 1 + \exp[(r - R_p)/a_p] \} .$$

The position of the center of this notch is the R_p parameter and this can be varied over the whole radial region of the potential. In the present analysis we have kept $a_p = 0.1$ fm and varied R_p from 4 to 14 fm for the real and the imaginary parts separately and calculated the χ^2 . In Fig. 5 the χ^2 values are plotted as a function of the notch radius, $R_p (=R_{\text{notch}})$. It is seen that the χ^2 maxima occur at ~ 8.5 fm for the real part and ~ 9 fm for the imaginary part. These values are well inside the strong absorption radius of ~ 11 fm. This indicates an increased sensitivity of the potential about 2 fm inside R_{SA} . The full width at half maximum (FWHM) of the χ^2 vs R_p plot has a broader distribution for the real part compared to the imaginary part. From the figure it is possible to conclude that the ^{209}Bi nucleus appears effectively black to 50.5 MeV alpha particles inside of about 6 fm.

2. Discrete potential family ambiguity

It is well known that it is not possible to determine the real part of the potential uniquely from an analysis of low energy alpha scattering data. This is due to the discrete family ambiguity problem and in principle one can obtain several discrete potentials giving equally good fits to the data. This problem can be considerably reduced and the range in the choice of potential families narrowed to reasonable values if the data are available over an extensive angular range. It is interesting to determine the possible potential families which will be allowed by the present data measured over a large angular range. If the best potential, as discussed earlier, is taken as the zeroth family ($n=0$), the potentials for fam-

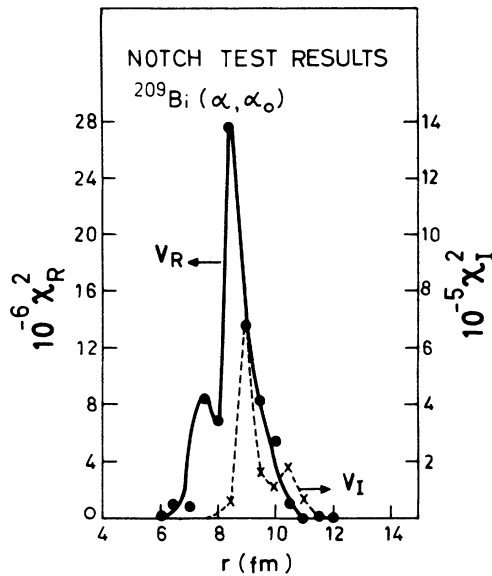


FIG. 5. The notch perturbation test: total χ^2 , summed over experimental points, as a function of the notch radius for the real and the imaginary parts of the potential. The solid and the dotted lines are guides to the eye connecting the χ^2 values for different values of r , calculated in the interval of 0.5 fm, for the real and the imaginary parts, respectively.

ilies with $n=1$ or $n=-1$ are given by the relation⁶

$$V_{\pm 1} = V_R \pm (h/R_S)[(E_{c.m.} + V_R - V_C)/2m]^{1/2} + h^2/8mR_S^2, \quad (17)$$

where $R_S = R_R(1 + \pi^2 a_R^2/R_R^2)^{1/3}$, m is the reduced mass, h is Planck's constant, and $V_C = 1.44Z_T \times 2/R_S$ MeV is the Coulomb potential. Similarly, we can get the $V_{\pm 2}$ families also. Using these values and R_R, a_R of the best fit family we can calculate the J_R values.

In the present work, we have made use of further constraints, requiring $R_{2.4}$ and S values for the various families to be equal to the corresponding best fit values. Once again by combining J_R , $R_{2.4}$, and S , we can generate the V_R , R_R , and a_R for the various families. We have used this alternate prescription for arriving at the parameters of the real part, rather than assuming R_R and a_R for the various families to be the same and equal to the corresponding best fit values. The present procedure is attractive in that we demand the potentials to be the same at $R_{2.4}$ (10.444 fm) which is very close to R_{SA} (11 fm).

Having fixed the real part by the above procedure, we kept the imaginary part fixed at the best value and calculated the χ^2 for various potential families. For completeness we also computed the χ^2 for potential sets which do not satisfy the family ambiguity condition for J_R but have the same $R_{2.4}$ and S . In Fig. 6 these results are plotted. The figure reveals the discrete ambiguity in the potential values. As expected the χ^2 values are large in

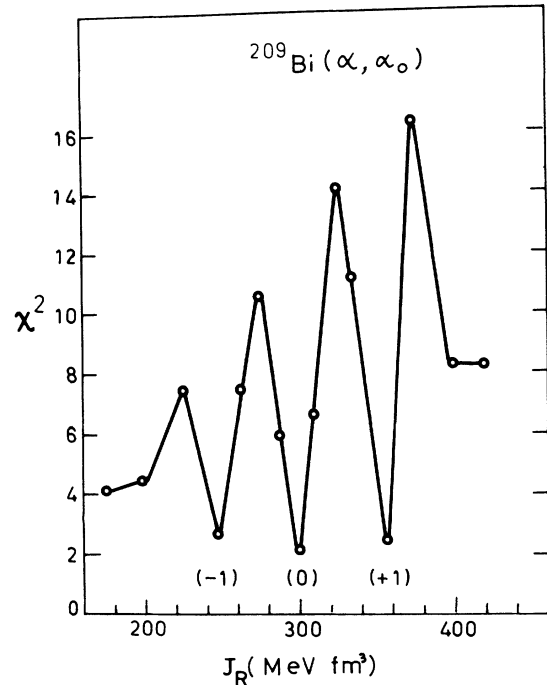


FIG. 6. Average χ^2 per point values plotted as a function of the volume integral of the real potential. The labels (-1) , (0) , $(+1)$ represent different discrete potential families as discussed in the text. The solid line is drawn to guide the eye.

between the various families. It appears that the present measurement has been able to restrict the potential to just three discrete families with $n=0, \pm 1$. This could possibly be because, in addition to the extensive angular range measured, we also have reasonably small error bars on the data at large angles.

3. Nearest-farside decomposition

The angular distribution shown in Fig. 1 has a Fresnel diffraction pattern in the forward angular range and a Fraunhofer pattern at the back angles. It has been shown^{11,12} that a decomposition of the data into the far-side and nearside components helps in filtering out the strong (but less sensitive to optical parameters) Fresnel part and enhances the relatively weak (but most sensitive to optical parameters) Fraunhofer part. This technique is a good handle to get at the reaction process taking place.

The elastic scattering amplitude is given by

$$f(\theta) = f_R(\theta) + \tilde{f}(\theta), \quad (18)$$

where f_R and \tilde{f} are the Rutherford and the nuclear parts, respectively. Both these components are divided into the far (F) and near (N) amplitudes so that

$$f_{N(F)}(\theta) = f_{R,N(F)}(\theta) + \tilde{f}_{N(F)}(\theta), \quad (19)$$

where

$$\tilde{f}_{N(F)}(\theta) = (2ik)^{-1} \sum_l (2l+1) e^{2i\sigma_l} (\tilde{S}_l - 1) \tilde{Q}_l^{(\mp)}(\cos\theta), \quad (20)$$

in which σ_l is the Coulomb phase shift, \tilde{S}_l is the optical model S matrix and $\tilde{Q}_l^{(\mp)}$ are the traveling-wave components¹⁶ of the Legendre polynomials,

$$P_l(\cos\theta) = \tilde{Q}_l^{(+)} + \tilde{Q}_l^{(-)}. \quad (21)$$

Following Fuller,¹¹ the far and near components of the Rutherford scattering amplitudes are calculated as

$$\begin{aligned} f_{R,N}(\theta)/f_R(\theta) \\ = [1 - \exp(-2\pi\eta)] - (i/2\pi) [\sin^2\theta/2]^{1+i\eta} S(\theta), \end{aligned} \quad (22)$$

$$\begin{aligned} f_{R,N}(\theta)/f_R(\theta) = -\exp(-2\pi\eta) [1 - \exp(-2\pi\eta)] \\ + (i/2\pi) [\sin^2\theta/2]^{1+i\eta} S(\theta), \end{aligned} \quad (23)$$

where

$$S(\theta) = (1+i\eta)^{-1} F(1, 1+i\eta, 2+i\eta; \sin^2\theta/2), \quad (24)$$

in which F is the hypergeometric function defined in Ref. 17. Defining

$$\sigma(\theta) = \sigma_N(\theta) + \sigma_F(\theta) + 2(\sigma_N\sigma_F)^{1/2} \cos(N,F), \quad (25)$$

where (N,F) is the phase difference between the near and the far amplitudes, we get

$$\sigma/\sigma_N = 1 + \sigma_F/\sigma_N + 2(\sigma_F/\sigma_N)^{1/2} \cos(N,F). \quad (26)$$

In Fig. 7 we compare σ/σ_N for the optical model and the experimental cross sections. It is evident that the oscillations which were less clearly seen in the σ/σ_R plot stand out rather prominently in the figure. The Fraunhofer oscillations arise due to the interference of the near and the far components. By presenting the data in this way the quality of the fit to the data can be judged much better.

The oscillations observed in Fig. 7 have a regular periodicity of $\Delta\theta \sim 9^\circ$. This quantity is related to the wave number k and radius R as $\Delta\theta = \pi/(kR)$. Expressing $\Delta\theta$ in radians, and using $k \sim 3 \times 10^{-13} \text{ cm}^{-1}$, we calculate R to be $\sim 7 \text{ fm}$. This value of R is close to the rms radii of the real and imaginary parts of the best-fit potential.

B. Inelastic scattering

The measured inelastic scattering cross sections to the states with excitation energies $E^* \approx 2.60 \text{ MeV}$ and 4.22 MeV are shown in Fig. 2. As the yields for inelastic scattering from the other states were small, they have not been considered for quantitative analysis.

The inelastic scattering data have been analyzed in terms of the collective-DWBA model, using the distorted waves generated from the optical potential deduced from the elastic scattering data. The cross sections calculated using the code¹⁸ DWUCK4 are also shown in Fig. 2.

The relative cross sections for the $E^* \approx 2.60 \text{ MeV}$

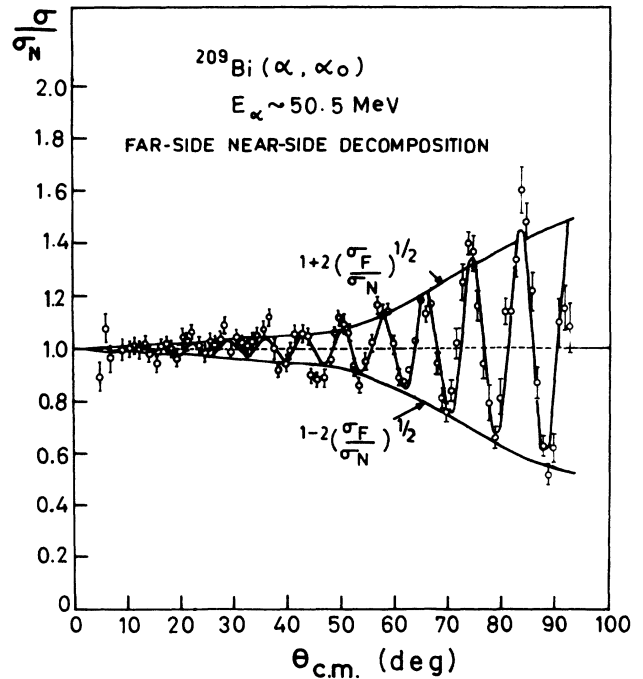


FIG. 7. The ratio of the experimental cross sections to the calculated nearside cross sections plotted as a function of the center-of-mass angle (points) compared to the optical model predictions (solid line). The calculated values of $1 \pm 2(\sigma_F/\sigma_N)^{1/2}$ are drawn as envelopes. (See text for details.)

group of states were well reproduced by the $l=3$ DWBA calculation and the deformation parameter was determined as $\beta_3=(\sigma_{\text{exp}}/\sigma_{\text{DWBA}})^{1/2}$. Taking $R=8.30$ fm (the mean of the real and imaginary potential radii) the deformation length was calculated as

$$\beta_3 R (E^* \approx 2.60 \text{ MeV}) = (0.71 \pm 0.05) \text{ fm} .$$

For the (α, α') reaction at 42 MeV (Ref. 19) a value of (0.75 ± 0.04) fm has been reported, with the data analyzed in terms of the Austern-Blair model. Electron scattering measurements²⁰ report a value of (0.81 ± 0.03) fm for this state. In high resolution (p, p') studies,²¹ the components of this state have been resolved with excitation energies ranging from 2.49 to 2.74 MeV. The combined $\beta_3 R$ value (adding the intensities) is 0.89 fm.

For the states centered around $E^* \approx 4.22$ MeV, it was found that the measured cross sections were best reproduced with a combination of the DWBA calculations for $l=2$ and $l=4$. The deformation lengths were calculated as

$$\beta_2 R (E^* \approx 4.22 \text{ MeV}) = (0.31 \pm 0.03) \text{ fm} ,$$

$$\beta_4 R (E^* \approx 4.22 \text{ MeV}) = (0.20 \pm 0.07) \text{ fm} .$$

The DWBA model fit to our data did not improve by attempting to include $l=3$ in the analysis; however, it is possible to include $l=3$ with a $\beta_3 R$ value up to 0.23 fm without any appreciable change in the quality of the fit. In the high-resolution (p, p') work,²¹ several states have been identified in this excitation energy region. The combined deformation length of the levels ranging in E^* from 4.09 to 4.36 MeV are $\beta_2 R=0.28$ fm, $\beta_3 R=0.33$ fm, and $\beta_4 R=0.35$ fm. The results from the present work are broadly consistent with those from Ref. 21 except

that our data are not sensitive to the $l=3$ contribution around this E^* region.

IV. CONCLUSIONS

In the present study of the $^{209}\text{Bi} + ^4\text{He}$ system it has been shown that a reasonable set of initial values for the optical model parameters can be obtained by extrapolating from the parameters at high energy, by using the systematics of the volume integral (J), the radius where the potential becomes 2.4 MeV ($R_{2.4}$), and the slope (S) at $r=R_{2.4}$ both for the real and the imaginary parts of the potential. Furthermore, it has been shown that for accurate measurements of the elastic cross sections over a wide angular range, the number of acceptable potential families can be restricted. The present measurement allows only three acceptable families.

The notch perturbation test has revealed that the sensitive region of the potential is around 8.5 and 9 fm for the real and the imaginary parts, respectively. These values are about 2 fm inside the strong absorption radius. The decomposition of the elastic scattering data into nearside and farside components has enabled the data to be presented in a way in which the large-angle Fraunhofer oscillations are prominent.

The deformation lengths (βR), deduced from a DWBA analysis of the inelastic data using the parameters determined from the elastic scattering analysis, are in general agreement with those obtained from other measurements in the literature.

We thank the staff of the Variable Energy Cyclotron, Calcutta, for the operation of the machine, R. P. Sharma for the supply of detectors, and Dr. S. N. Chintalapudi and S. Bhattacharya for their help in the initial stages of the experiment.

¹P. P. Singh and P. Schwandt, *Nukleonika* **21**, 451 (1976); in *Proceedings of the 2nd Louvain-Cracow Seminar, Louvain-la-Neuve, 1978*, edited by G. Gregoire and K. Grotowski (Institut Internuniversitaire Des Sciences Nucleaires Universite De Louvain, Louvain-la-Neuve, 1978).
²H. Dabrowski and L. Friendl, *Acta Phys. Pol. B* **12**, 703 (1986).
³D. A. Goldberg, S. M. Smith, and G. F. Burdzik, *Phys. Rev. C* **10**, 1362 (1974).
⁴G. Igo, *Phys. Rev.* **115**, 1665 (1959).
⁵R. M. Drisko, G. R. Satchler, and R. H. Basel, *Phys. Lett.* **5**, 347 (1963); M. E. Cage, A. J. Cole, and G. J. Pyle, *Nucl. Phys. A* **201**, 418 (1973).
⁶H. H. Chang, B. W. Ridley, T. H. Braid, T. W. Conlon, E. F. Gibson, and N. S. P. King, *Nucl. Phys. A* **270**, 413 (1976).
⁷S. K. Gupta and K. H. N. Murthy, *Z. Phys. A* **307**, 187 (1982).
⁸S. Kailas, S. K. Gupta, S. Bhattacharya, S. N. Chintalapudi, and Y. P. Viyogi, *Pramana J. Phys.* **23**, 495 (1984).
⁹A. Sridhar, N. Lingappa, S. K. Gupta, and S. Kailas, *Phys. Rev. C* **30**, 1760 (1984).

¹⁰J. G. Cramer and R. M. DeVries, *Phys. Rev. C* **22**, 91 (1980).
¹¹R. C. Fuller, *Phys. Rev. C* **12**, 1561 (1975).
¹²M. S. Hussein and K. W. McVoy, *Prog. Part. Nucl. Phys.* **12**, 103 (1984).
¹³S. K. Gupta, *Nucl. Instrum. Methods A* **239**, 152 (1985).
¹⁴P. Schwandt, Indiana University Cyclotron Facility Report No. 81-3, 1981 (unpublished).
¹⁵C. M. Perey and F. G. Perey, *At. Data Nucl. Data Tables* **17**, 1 (1976).
¹⁶R. C. Fuller and K. W. McVoy, *Phys. Lett.* **55B**, 121 (1975).
¹⁷*Handbook of Mathematical Functions*, edited by M. Abramowitz and I. Stegun (U.S. GPO, Washington, D.C., 1964).
¹⁸P. D. Kunz, University of Colorado report, 1982 (unpublished).
¹⁹J. Alster, *Phys. Rev.* **141**, 1138 (1966); *Phys. Lett.* **25B**, 459 (1967).
²⁰J. F. Ziegler and G. A. Peterson, *Phys. Rev.* **165**, 1337 (1968).
²¹W. T. Wagner, G. M. Crawley, and G. R. Hammerstein, *Phys. Rev. C* **11**, 486 (1975).